Thermodynamic Aspects of the Constitution, Grain Refining, and Solidification Enthalpies of Al-Ce-Si Alloys

JOACHIM GRÖBNER, DJORDJE MIRKOVIĆ, and RAINER SCHMID-FETZER

The ternary Al-Ce-Si phase equilibria were investigated using X-ray diffraction (XRD) methods, metallography, scanning electron microscopy with energy-dispersive X-ray analysis (SEM/EDX) and wavelength-dispersive X-ray microanalysis, and differential thermal analysis (DTA). The focus was on the Al-rich corner and the phases in equilibrium with (Al). Key experiments were selected by preliminary thermodynamic calculations. A consistent thermodynamic description was developed using the Calphad method incorporating all experimental data. A thermodynamic assessment for the binary Ce-Si system was also performed. Two ternary phases, $Ce(Si_{1-x}Al_x)_2$ (τ_1) and $AlCeSi_2$ (τ_2), were confirmed. The phase Al_2CeSi_2 (τ_4) was sporadically observed, but is apparently metastable. The earlier reported phase $Al_4Ce_3Si_6$ could not be confirmed. In addition, the enthalpy of solidification of five Al-rich ternary alloys was measured in a differential scanning calorimetry (DSC) heat flux calorimeter. The agreement with the thermodynamic enthalpy calculations is acceptable. The fundamental intricacies involved in calculating a "latent" heat for alloys with a freezing range are pointed out. Various phase diagrams of the Al-Ce-Si system were calculated based on the thermodynamic description. They were used to quantitatively identify possible contributions to the grain refinement potential of Ce in Al-Si alloys due to the phase equilibria.

I. INTRODUCTION

ALUMINUM alloys with Si as the major alloying element are the most important Al-based foundry alloys because of their excellent casting characteristics, weldability, pressure tightness, and corrosion resistance.[1] The final properties of the castings are considerably affected by the morphology of the primary solidified phases, which is valid for both primary (Al) solid solution (hypoeutectic alloys containing less than 12 mass pct Si) and primary (Si) crystals (hypereutectic Al-Si alloys). Grain refining is an important technique to exert control over this morphology. It is used to improve mechanical strength, ductility, homogeneity, feeding during solidification, and other desired properties of the Al-Si casting alloys. This is of the utmost importance for the sand and permanent mold castings due to lower cooling rate compared to pressure die casting.

Despite the voluminous literature on grain refinement, there is no consensus on the mechanism of grain refinement in Al alloys.[2] The most important models suggested to explain grain refinement are the "nucleant paradigm," purely being concerned with the nucleation event, and the "solute paradigm," considering also the effect of solute elements on grain growth. A shift from the first attitude in understanding grain refining to the second one has been noticed in recent years.[2,3]

An established practical grain refining procedure for hypoeutectic Al-Si alloys is the addition of Al-Ti-B master alloys, and there is extensive literature examining the influence of this refiner on the microstructure of the casting. These master alloys, however, are not applicable to hypereutectic Al-Si alloys. The reason suggested is a poisoning effect of titanium silicide on the $TiAl_3$ nucleation site, which is observed if the Si content is higher than 7 mass pct.[1,4] Grain refinement in hypereutectic Al-Si alloys is particularly needed since the primary (Si) is usually very coarse, resulting in poor mechanical properties. Addition of phosphorus as an Al-P master alloy to the melt is widely used, thus forming high-temperature stable Al phosphides that act as nucleation sites for primary (Si) crystals.[5,6] This practice is rather controversial due to long necessary dwell time, high amount of P addition, pollution of the furnace walls, and environmental aspects.

An alternative, which has not been well investigated, is the addition of rare earth (RE) metals as a grain refiner. In a hypereutectic Al-21Si alloy, Chang *et al*.[7] observed simultaneous refinement of both primary and eutectic Si using RE mischmetal additions. The concentration of RE in primary (Si) and the enriched matrix was also studied by Chang *et al*.[8] and the few earlier reports on the effect of RE additions are reviewed.[7,9] However, the actual grain refining mechanisms are still unclear.

The purpose of this study is to provide basic thermodynamic and constitutional data needed to assess the grain refinement potential of RE metals, here represented by cerium, a main constituent of commercial mischmetal alloys. To this end, the ternary Al-Ce-Si phase equilibria were studied by combining thermodynamic modeling with key experiments, including calorimetric determination of solidification enthalpies of ternary alloys and the thermodynamic assessment of the missing Ce-Si binary system.

II. THE BINARY SYSTEM Ce-Si

The binary phase diagram is based on the work of Benesovsky *et al*.[10] Their samples were prepared using cerium hydride (99.5 pct purity) and Si (99.7 pct purity).

JOACHIM GRÖBNER, Postdoctoral Fellow, DJORDJE MIRKOVIĆ, Graduate Student, and RAINER SCHMID-FETZER, Professor, are with the Institute of Metallurgy, University of Clausthal, D-38678 Clausthal-Zellerfeld, Germany. Contact e-mail: schmid-fetzer@tu-clausthal.de

Manuscript submitted January 29, 2004.

The powder mixtures were cold pressed and heated in tungsten-tube vacuum furnace for 5 to 20 hours at 850 °C to 1300 °C. Afterward, the alloys were investigated by X-ray powder diffraction (XRD). The melting temperatures were determined by observing the melting of Seger-cone-formed samples in tungsten-tube vacuum furnace under He atmosphere. The temperature was measured using a micropyrometer. Six intermediate phases were found with corresponding melting temperatures: Ce_5Si_3 (1400 °C), Ce_3Si_2 (1390 °C), Ce_5Si_4 (1440 °C), CeSi (1470 °C), Ce_3Si_5 (1560 °C), and $CeSi_2$ (1620 °C). Six eutectic reactions and a peritectic reaction were concluded from the results. Information about the number of samples and their composition is not given. The phase diagram of Benesovsky *et al.*[10] was later modified by Gschneider and Verkade.[11] There are no reliable solid solubility data available in the literature. Benesovsky *et al.*[10] rather speculatively indicated a small (1.2 at. pct) range of mutual solid solubility. In other RE-Si binary systems, the mutual solid solubilities are very small.[12]

The presence of additional phases, Ce_3Si[13] and $CeSi_{0.75}$,[14] are considered questionable because they were not confirmed by other authors. The two intermediate phases $CeSi_{2-x}$ and $CeSi_2$ reported by Benesovsky *et al.*[10] crystallized in the same $\alpha ThSi_2$-type structure and are most probably part of a homogeneity range between 64 and 66.67 at. pct Si. The presence of a homogeneity range for $CeSi_2$ is also supported by Yashima *et al.*[15]

The standard enthalpies of formation of the phases CeSi, $CeSi_2$,[16] and Ce_5Si_3[17] have been determined by direct-synthesis calorimetry at 1200 °C ± 2 °C and are given in Table I. The enthalpy of mixing in the Ce-Si binary liquid has been measured by Ryss *et al.*[18,19] at 1650 °C and Sudavtsova *et al.*[20] at 1617 °C using isothermal calorimetry. They also derived partial enthalpy of mixing data from their measurements.

A. *Thermodynamic Calculation of the Binary Ce-Si System*

The Gibbs energy function $G_i^{0,\varphi}(T) = G_i^{\varphi}(T) - H_i^{SER}$ for the element i (i = Al, Ce, Si) in the ϕ phase (ϕ = fcc (Al, αCe), bcc (βCe), diamond (Si), and liquid) is described by the equation

$$G_i^{0,\varphi}(T) = a + b\cdot T + c\cdot T\cdot \ln T + d\cdot T^2 + e\cdot T^3 + f\cdot T^{-1} + g\cdot T^7 + h\cdot T^{-9} \quad [1]$$

where H_i^{SER} is the molar enthalpy of the stable element reference (SER) at 298.15 K and 1 bar, and T is the absolute temperature. The Gibbs energy functions for Al, Ce, and Si are taken from the SGTE compilation by Dinsdale.[21]

The binary thermodynamic parameters were optimized with the programs WinPhad/Pandat.[22] The enthalpies of formation for the intermediate phases were essentially taken from Meschel and Kleppa,[16,17] as detailed in Table I, and phase diagram data after Benesovsky *et al.*[10] were used. The six intermetallic phases were modeled as stoichiometric compounds Ce_xSi_y referred to the stable elements by

$$G^{Ce_xSi_y} = xG_{Ce}^{0,fcc}(T) + yG_{Si}^{0,diamond}(T) + A_{xy} + B_{xy}\cdot T \quad [2]$$

where the parameters A_{xy} and $(-B_{xy})$ correspond to the enthalpy and entropy of formation. Liquid was modeled as a subregular solution with two linearly temperature-dependent parameters, L^0 and L^1, as expressed by the following equation:

$$G^{Liq} = x_{Ce}G_{Ce}^{0,Liq} + x_{Si}G_{Si}^{0,Liq} + RT(x_{Ce}\ln x_{ce} + x_{Si}\ln x_{si}) + x_{Ce}x_{Si}(L^{0,Liq} + L^{1,Liq}(x_{Ce} - x_{Si})) \quad [3]$$

in which R is the gas constant and x_{Ce} and x_{Si} are the molar fractions of Ce and Si.

The solubilities of Ce in (Si) and of Si in (Ce) were neglected since no data for the solubilities are available and the solid solubilities are expected to be very small. The phase $CeSi_2$ was approximated by a line compound even though a small solubility range from 64 to 66.67 at. pct Si was reported.[10] The resulting calculated phase diagram with the experimental data from Benesovsky *et al.*[10] inserted as symbols is given in Figure 1.

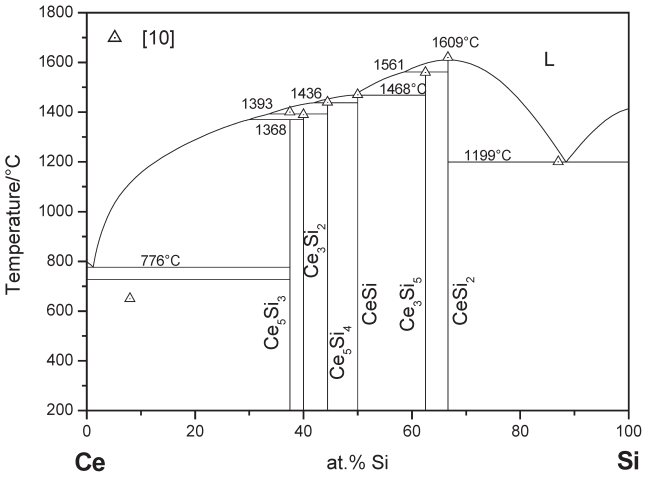

Fig. 1—Calculated phase diagram of the binary Ce-Si system with the experimental data.[10] The homogeneity range of $CeSi_2$ (64 to 66.67 at. pct Si) is simplified to the stoichiometric composition in the present calculation.

Table I. Standard Enthalpies of Formation of the Intermediate Binary Ce-Si Phases at 298 K (for Reference States, see Equation [2]) and Absolute Entropies at 298 K

Quantity	Ce_5Si_3	Ce_3Si_2	Ce_5Si_4	CeSi	Ce_3Si_5	$CeSi_2$	Method/Reference
$\Delta_f H^0$ (kJ/mol atoms)	—	—	—	−71.1 ± 3.3	—	−60.5 ± 2.0	calorimetry[16]
$\Delta_f H^0$ (kJ/mol atoms)	−52.8 ± 0.6	—	—	—	—	—	calorimetry[17]
$\Delta_f H^0$ (kJ/mol atoms)	−61.0	−65.0	−69.0	−71.1	−65.0	−60.5	Calphad assessment, this work
S^0_{298} (J/mol atoms K)	46.6	44.1	42.3	40.7	41.3	41.5	Calphad assessment, this work

III. THE TERNARY SYSTEM Al-Ce-Si

A. *Experimental Literature Data of the Ternary System Al-Ce-Si*

Early investigations on the Al-Ce-Si ternary system cover only the Ce-poor region from 0 to 33 at. pct Ce.[23–29] A first isothermal section in that range at 400 °C was given by Zarechnyuk[24] and Altunina *et al*.[25] derived from the results of X-ray powder diffraction, metallography, and in some cases chemical analysis. The samples were prepared by melting Al (99.99 pct purity) and Ce (99.567 pct purity) in an alumina crucible under a protective layer of a mixture of KCl + LiCl. The alloys were annealed for 50 to 100 hours at 400 °C and the 25 alloys in the Al-rich region at 500 °C. They reported the existence of one ternary compound with a nominal composition Ce20Al35Si45 (at. pct) and a composition range for mixed crystals $CeAl_xSi_{2-x}$ ($\alpha ThSi_2$ type) extending up to 60 at. pct Al or $x = 1.8$. Raman *et al*.[26,27] observed the formation of a ternary phase of the different AlB_2 type in a ternary alloy $CeAl_{1.625}Si_{0.375}$, which contradicts the wide composition range of $CeAl_xSi_{2-x}$, suggested by previous researchers.[24,25] In the studies by Raman *et al*.,[26,27] the alloy was prepared by arc melting the elements of 99.9 pct minimum purity and wrapped in molybdenum foil after melting, which was followed by heating in evacuated silica capsules at 1000 °C for 96 hours and slow cooling in air. The existence of this ternary phase was later confirmed by Murav'eva[28] at 500 °C in an investigation of the phase equilibria for the 0 to 33 at. pct Ce section of the Ce-Al-Si system using X-ray powder diffraction and metallographic analysis of 65 alloys, which were arc melted and subsequently annealed for 150 to 750 hours at 500 °C in evacuated silica tubes. The starting materials were 99.0 pct pure Ce and 99.90 pct pure Al and Si. Two additional ternary phases were reported by Murav'eva *et al*.[29] at 500 °C. The crystallographic data of all ternary phases are listed in Table II.

Flandorfer and Rogl[30] described the crystal structure of two compounds: $AlCeSi_2$ and $Al_4Ce_3Si_6$. The samples were synthesized by arc melting and investigated analyzing X-ray data *via* Patterson and Fourier methods followed by full-matrix Rietveld refinement. The phase with the composition $Al_4Ce_3Si_6$ appears after long annealing (336 hours) of arc-melted Al_2CeSi_2 alloy at 500 °C. The phase with the composition Al_2CeSi_2, τ_4, reported in References 28 and 29 is found to be disappearing after annealing at 700 °C, 600 °C, and 500 °C und therefore was considered to be metastable by the researchers,[30] as given in Table II. The Ce-poor region (≤33 at. pct Ce) of the isothermal section at 600 °C was investigated by Flandorfer *et al*.[31] The samples were synthesized by argon arc melting using starting materials of high purity. After melting, the samples were packed in Mo foil, sealed in evacuated silica tubes, and heat treated at 600 °C. All samples were analyzed by X-ray diffraction (XRD) and refined by Rietveld full matrix technique. Flandorfer *et al*.[31] confirmed the stability of three ternary phases τ_1, τ_2, and τ_3 at 600 °C. After all these investigations, two three-phase equilibria are established in the Al-rich corner: (1) (Al) + $Al_{11}Ce_3$ + τ_1 and (2) (Al) + τ_1 + τ_2. We will stick to the notation of τ_1 for the phase $Ce(Si_{1-x}Al_x)_2$, although this phase is not a true ternary compound since it develops—at least at high temperature—as a solution from the binary $CeSi_2$ phase.

Table II. Solid Ternary Phases Occurring in the Al-Si-Ce System

Phase	Structure Type, Pearson Symbol, Space Group	Lattice Parameters (nm) *a*	*b*	*c*	Comment, Reference
τ_1 $Ce(Si_{1-x}Al_x)_2$	$\alpha ThSi_2$ *tI*12 $I\bar{4}_1$ *amd*				solid solution, $x = 0$ to 1[28] miscibility gap at 500 °C from $x \approx 0.1$ to 0.9[28]
		0.4192	—	1.390	at $x = 0$[38]
		0.4150(5)	—	1.3870(1)	at $x = 0$ and 1000 °C[27]
		0.4185	—	1.388	at $x = 0$ and 400 °C[24,25]
		0.432	—	1.5200	at $x = 0.9$ and 400 °C[24,25]
		0.425	—	1.454	at $Al_{1.4}CeSi_{0.6}$, 500 °C[28]
		0.427	—	1.492	at $Al_{0.9}CeSi_{1.1}$, 500 °C[28]
		0.4280(5)	—	1.490(1)	at $Al_{1.5}CeSi_{0.5}$, 1000 °C[28]
τ_2 $AlCeSi_2$	$Ce_2Al_3Si_5$ *hR*10 or	0.385	—	0.947	at $Al_{1.25}CeSi_{2.75}$, 500 °C[28]
	$AlCeSi_2$ *hP*8 $P\bar{3}m1$	0.41707(1)	—	1.12147(2)	at 600 °C[30]
τ_3 Al_xCeSi_{2-x}	AlB_2 *hP*3 *P6mmm*	0.435	—	0.430	$1.55 < x < 1.64$[28]
		0.432	—	0.443	at $Al_{1.64}CeSi_{0.36}$, 500 °C[28]
		0.4315(5)	—	0.4298(5)	at $Al_{1.55}CeSi_{0.45}$, 500 °C[28]
					at $Al_{1.625}CeSi_{0.375}$, 1000 °C[26,27]
τ_4 Al_2CeSi_2	La_2O_2S	0.421	—	0.694	at 500 °C[28,29]
	(La_2O_3) *hP*5 $P\bar{3}m1$	0.4217(0)	—	0.6895(1)	metstable[30] metastablility confirmed (this work)
τ_5 $Al_4Ce_3Si_6$	$Al_4Ce_3Si_6$ *hP*13 $P\bar{3}m1$	0.41887(1)	—	1.81202(6)	after long annealing (336 h) at 500 °C[30] not found after 870 h at 500 °C (this work) 500 °C (this work)

B. *Experimental Investigation*

The present experimental investigation of the Al-Ce-Si phase equilibria was carried out with XRD analysis, metallographic analysis, scanning electron microscopy with energy-dispersive X-ray microanalysis (SEM/EDX), differential thermal analysis (DTA), and differential scanning calorimetry (DSC). Nine samples with compositions given in Table III were prepared.

Starting materials were Al foil (99.997 mass pct, Alfa, Karlsruhe), Ce pieces (99.9 mass pct, Santoku America Inc., Phoenix, AZ), and Si chips (99.9998 mass pct, Wacker, Burghausen). The Ce pieces and the Si chips were wrapped in Al foil and carefully arc melted under purified argon. The loss in total mass was below 2 pct for all samples that went to further analysis. For all compositions, as-cast and heat-treated samples were prepared. Samples for heat treatment were put in silica tubes, repeatedly evacuated down to $4 \cdot 10^{-2}$ mbar and flushed with argon, sealed under vacuum, and heat treated at 500 °C for 870 hours. These samples were water quenched.

The heat-treated Al-poor samples ($Al_{58.9}Ce_{20.5}Si_{20.6}$, $Al_{35}Ce_{20}Si_{45}$, $Al_{40}Ce_{20}Si_{40}$, and $Al_{45}Ce_{25}Si_{30}$, at. pct) were powdered in a steel ball mill for investigation by XRD to determine the phases present. The measurements were performed using a Siemens D5000 (Bruker AXS, Karlsruhe, Germany) diffractometer with a step 0.02 deg of 2θ and 3 seconds exposition time in the point.

For the DSC and DTA analysis, two samples for each alloy composition were prepared and two measurement cycles were performed for each sample. Five alloys in the Al-rich corner with compositions $Al_{90.0}Ce_{8.0}Si_{2.0}$, $Al_{90.0}Ce_{7.0}Si_{3.0}$, $Al_{90.0}Ce_{5.7}Si_{4.3}$, $Al_{90.0}Ce_{3.2}Si_{6.8}$, and $Al_{90.0}Ce_{2.6}Si_{7.4}$ were studied by DSC. Both the reaction temperatures and the solidification enthalpy were measured by DSC in a heat-flux twin cylindrical Calvet-type calorimetric system, Setaram MHTC 96 (Setaram, Caluire, France). Before performing the experiment, the equipment was calibrated using Ag, Al, Au, In, Pb, and Sn. Helium at 2 L/h flow rate has been applied as the analysis chamber gas. For all measurements, the sample and reference cells were built as alumina sleeves, covered with a lid, which were inserted in Pt crucibles. In order to position the sample approximately in the middle of the cell height in the most sensitive zone, the sample alumina sleeve was filled with about 135 mg water-free γ-Al_2O_3 powder before the sample was inserted. The reference alumina sleeve was filled with the same amount of the water-free γ-Al_2O_3 powder (± 1 mg tolerance), but otherwise left empty. The DSC measurements were carried out with heating/cooling rates of 2 and 5 K/min. A typical sample weight was about 150 mg. The overall uncertainty of DSC measurements was estimated as ± 3 K and ± 0.3 kJ/mol atoms for temperature and enthalpy determination, respectively.

Outside the Al-rich corner, the three samples with the compositions $Al_{35}Ce_{20}Si_{45}$, $Al_{40}Ce_{20}Si_{40}$, and $Al_{45}Ce_{25}Si_{30}$ (at. pct) were studied by DTA performed in a Netzsch DTA 404S (Netzsch-Gerätebau GmBH, Selb, Germany) apparatus. The samples were inserted in an alumina crucible closed by a lid. As the reference cell, an identical, though empty, alumina crucible with a lid was used. Prior to the measurements, the analysis chamber was three times evacuated down to 7×10^{-3} mbar and flushed with Ar, purified by a Millipore filter (less than 1 ppb oxygen) (Millipore, Billerica, MA). By the last flushing, the pressure was set to 933 mbar under static pressure. The heating/cooling rates applied were 1 and 5 K/min. The overall uncertainty of DTA measurements was estimated as ± 4 K.

The microstructures of the samples after arc melting (as-cast), after heat treatment and after slow cooling in DSC/DTA experiments, were examined by scanning electron microscopy. The samples were ground and polished down to 1-μm diamond paste under alcohol to avoid reaction with water. Etching was not necessary.

C. *Experimental Results*

Table III shows the phase assembly of all investigated samples derived from XRD, metallographic, and SEM/EDX analysis. Primary crystallizing phases detected from their morphology in as-cast solidified microstructure are given in the last column. Crystallographic data of solid phases occurring in the ternary Al-Ce-Si system are given in Table II. Two ternary phases, $Ce(Si_{1-x}Al_x)_2$ (τ_1) and $AlCeSi_2$ (τ_2), were definitely found by both SEM/EDX and XRD analyses. The phase Al_2CeSi_2 (τ_4) was sporadically observed in the microstructure of the annealed samples with composi-

Table III. Sample Compositions and Phase Assembly Derived from X-Ray, Metallographic, and SEM/EDX Analysis in This Work

Sample Composition in At. Pct	Phases Identified by XRD	Phases Identified by SEM/EDX	Phases Primary Crystallized
$Al_{90.0}Ce_{8.0}Si_{2.0}$	—	$Al_{11}Ce_3 + \tau_1 + (Al)$	$Al_{11}Ce_3$
$Al_{90.0}Ce_{7.0}Si_{3.0}$	—	$Al_{11}Ce_3 + \tau_1 + (Al)$	τ_1
$Al_{90.0}Ce_{5.7}Si_{4.3}$	—	$\tau_1 + Al_{11}Ce_3 + (Al)$	τ_1
$Al_{90.0}Ce_{3.2}Si_{6.8}$	—	τ_1** + τ_4† + (Al)	τ_1
$Al_{90.0}Ce_{2.6}Si_{7.4}$	—	τ_1** + τ_2 + (Al) + τ_4†	τ_1
$Al_{58.9}Ce_{20.5}Si_{20.6}$	τ_1‡ + (Al) + τ_3†	τ_1** + (Al)	τ_1
$Al_{35}Ce_{20}Si_{45}$	$\tau_1 + \tau_2$ + (Si)/(Al)	$\tau_1 + \tau_2$ + (Si) + (Al)	τ_1
$Al_{40}Ce_{20}Si_{40}$	$\tau_1 + \tau_2$ + (Al)§	$\tau_1 + \tau_2$ + (Al) + (Si)	τ_1
$Al_{45}Ce_{25}Si_{30}$	$\tau_1 + \tau_2$ + (Al)	$\tau_1 + \tau_2$ + (Al)	τ_1

*Samples studied by XRD were water quenched after annealing for 870 h at 500 °C. Samples studied by SEM/EDX were both as-cast and annealed/quenched. No significant difference in phase assembly was noticed between these two types of samples.

‡Peak shifted because of Al solubility.

**Wide solubility range.

†Probably not in equilibrium.

§Diffuse X-ray pattern.

tions $Al_{90.0}Ce_{3.2}Si_{6.8}$ and $Al_{90.0}Ce_{2.6}Si_{7.4}$, but not confirmed by XRD analysis of the annealed sample with the Al_2CeSi_2 ($Al_{40}Ce_{20}Si_{40}$) composition. The phase $Al_4Ce_3Si_6$, reported in Reference 30, could not be confirmed. The microstructures of the annealed samples show no additional phases compared to the as-cast alloys; only coarsening of the grains was observed.

The temperatures extracted from the DSC/DTA curves and their interpretation are summarized in Table IV. For the cooling curves, onset temperatures are determined. The heating peaks are interpreted according to the peak shape analysis; onset temperatures are determined for thermal signals related to invariant reactions, and otherwise peak maximum temperatures are evaluated. This interpretation follows established procedures.[32] Some thermal signals are weak and diffuse, as indicated. Quite often, the heating signals relating to not-invariant reactions, mainly the liquidus temperature, appeared diffuse and flat, thus impeding a clear determination of the peak maximum. An example is given in Figure 2. In such cases, the associated and more distinct cooling signal was considered more reliable and its onset temperature was adopted as the assessed experimental temperature in Table IV. Otherwise, the mean value of heating and cooling signals was taken. Cooling signals were checked for the shape of the initial peak rise, in order to recognize possible substantial undercooling and, if so, to exclude this signal from the assessment.

The thermal signals of the five samples along the section with constant 90 at. pct Al are displayed in Figure 3. Corresponding

Table IV. Temperatures Extracted from the DSC and DTA Curves Obtained by Thermal Analysis in the Al-Si-Ce System and Their Interpretation; Invariant Reactions Were Recognized from the Peak Shape

Sample Composition in At. Pct	Thermal Signal		Interpretation	
	Heating* (°C)	Cooling** (°C)	Experimental Temperature (°C)	Phase Boundary or Invariant Reaction
$Al_{90.0}Ce_{8.0}Si_{2.0}$	898 w	904 s	904	$L/L + Al_{11}Ce_3$
	not detected	729 w	729	?
	640 s	634 s	634	E_1
	633 w	not certain	633	?
$Al_{90.0}Ce_{7.0}Si_{3.0}$	845 w	851 s	851	$L/L + \tau_1$
	833 w	837 w	837	?
	639 s	633 s	633	E_1
	633 w	not certain	633	?
$Al_{90.0}Ce_{5.7}Si_{4.3}$	837 w	837 s	837	$L/L + \tau_1$
	not detected	667 w	667	?
	639 s	632 s	633	E_1
	633 w	not detected	633	?
$Al_{90.0}Ce_{3.2}Si_{6.8}$	not certain	783 s	783	$L/L + \tau_1$
	625 s	621 s	621	U_{11}
	598 w	616 w	616	?
	585 s	573 s	573	$\tau_1 + \tau_2 + (Al)/\tau_2 + (Al)$
	577 s	569 s	569	E_2?
$Al_{90.0}Ce_{2.6}Si_{7.4}$	760 w	762 s	762	$L/L + \tau_1$
	612 s	616 s	616	U_{11}
	601 w	609 w	609	?
	591 s	574 s	574	?
	577 s	570 s	570	E_2
$Al_{35}Ce_{20}Si_{45}$	1321 s	1317 s	1319	$L/L + \tau_1$
	1301 s	1300 s	1301	?
	not certain	1275 w	1275	?
	823 s	818 s	820	$L + \tau_1/L = \tau_1 + (Si)$?
	654 s	588 s	653	P_2
	613 s	575 s	613	U_{11}?
	587 w	572	587	?
	576 s	567 s	571	E_2
$Al_{40}Ce_{20}Si_{40}$	1284 w	1242 w	1260	$L/L + \tau_1$
	728 s	712 s	712	?
	652 s	613 s	651	$L + \tau_1/L = \tau_1 + (Al)$
	610 w	580 w	610	U_{11}
	574 w	573 w	574	?
	572 s	573 s	572	E_2
$Al_{45}Ce_{25}Si_{30}$	1212 w	not certain	1212	$L/L + \tau_1$
	590 s	589 s	590	U_{11}
	585 s	581 s	585	?
	571 w	not detected	571	?

*Onset for invariant reactions; peak maximum otherwise.
**Onset.
w = weak and diffuse signal.
s = strong and clear signal.

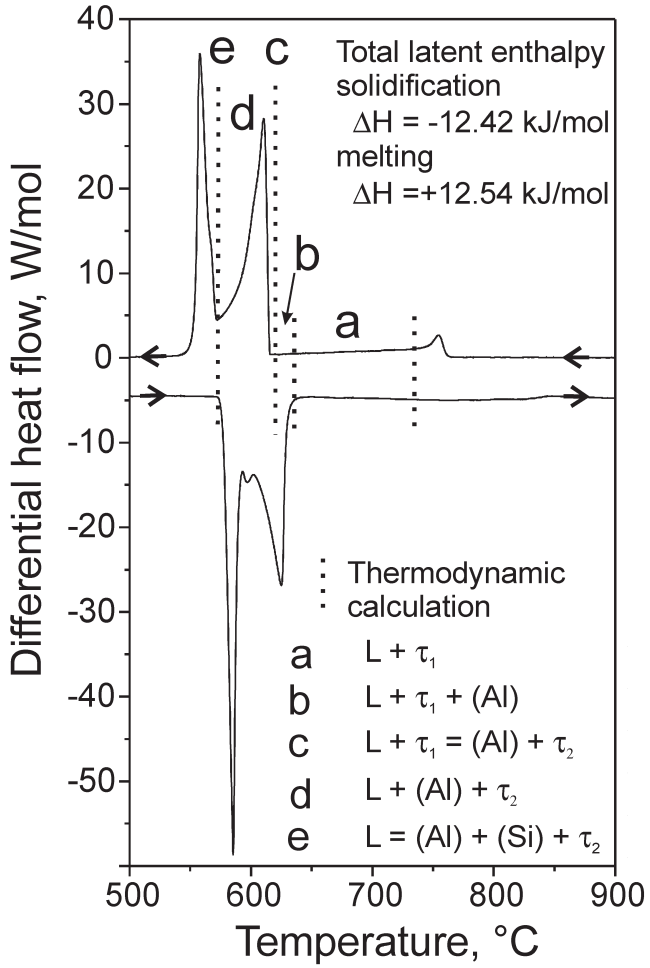

Fig. 2—DSC peaks during solidification and melting of the sample $Al_{90.0}Ce_{2.6}Si_{7.4}$ at a rate of 5 K/min. The calculated equilibrium phase boundaries are superimposed, as given also in Fig. 3.

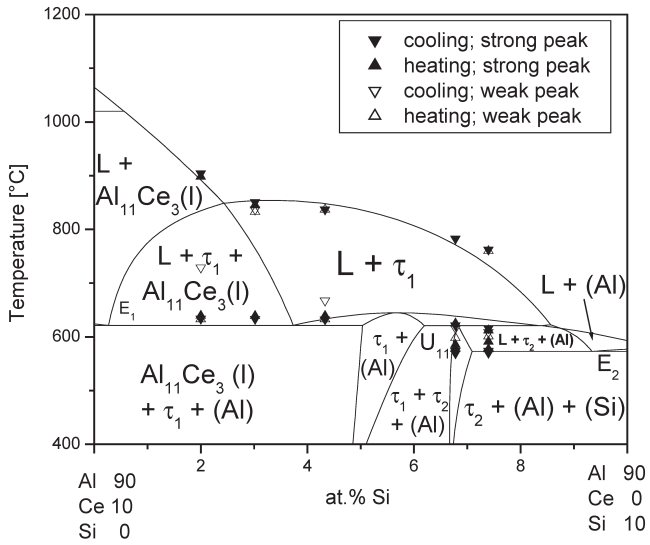

Fig. 3—Calculated vertical section $Al_{90}Ce_{10}$-$Al_{90}Si_{10}$ at constant 90 at. pct Al including the DSC/DTA signals measured in this work.

microstructures of the samples $Al_{90.0}Ce_{8.0}Si_{2.0}$, $Al_{90.0}Ce_{7.0}Si_{3.0}$, $Al_{90.0}Ce_{5.7}Si_{4.3}$, and $Al_{90.0}Ce_{2.6}Si_{7.4}$ are given in Figures 4 through 7. The sample's thermal histories are detailed in the captions. The mass contrast of backscattered electrons (BSE) shown in all figures makes the heavy Ce-richest phase τ_1 appear brightest and the (Al) in the eutectic matrix darkest. $Al_{11}Ce_3$ is the primary crystallized phase only in the Si-poorest sample (Figure 4); in all other samples, τ_1 is primary. The secondary phase can also be recognized clearly. The matrix of all samples consists of eutectic microstructure. It should be noted that the difference between the as-cast and the heat-treated microstructures is small and limited to the coarsening of the secondary crystals. No difference concerning the primary crystals and phase content is observed after heat treatment. In Figure 7, the electron micrograph of the sample

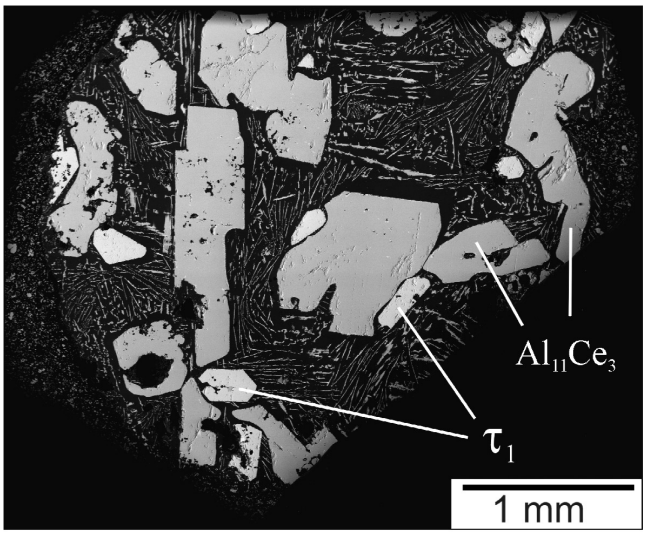

Fig. 4—Electron micrograph (BSE) of the sample $Al_{90}Ce_8Si_2$ (as-cast and subsequently 870 h at 500 °C) showing large crystals of primary $Al_{11}Ce_3$ (darker gray) associated with small crystals of τ_1 (light gray) in eutectic matrix.

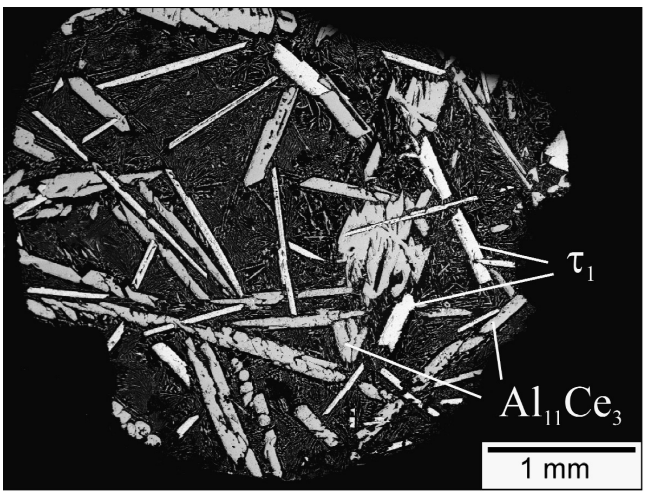

Fig. 5—Electron micrograph (BSE) of the as-cast sample $Al_{90}Ce_7Si_3$ after being solidified at 5 K/min cooling rate during DSC measurement. The primary crystallized phase τ_1 (light gray) and the secondary phase $Al_{11}Ce_3$ (darker gray) in eutectic matrix are observed.

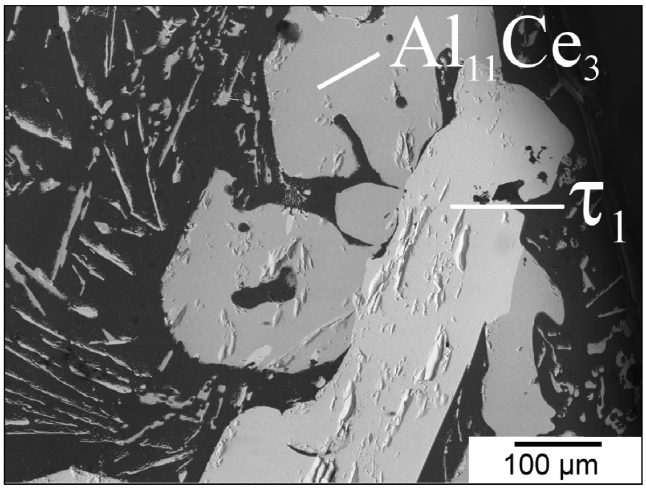

Fig. 6—Electron micrograph (BSE) of the sample $Al_{90.0}Ce_{5.7}Si_{4.3}$ (as-cast and subsequently 870 h at 500 °C) showing the detailed intergrowth of primary τ_1 (light gray) and $Al_{11}Ce_3$ (darker gray) in eutectic matrix.

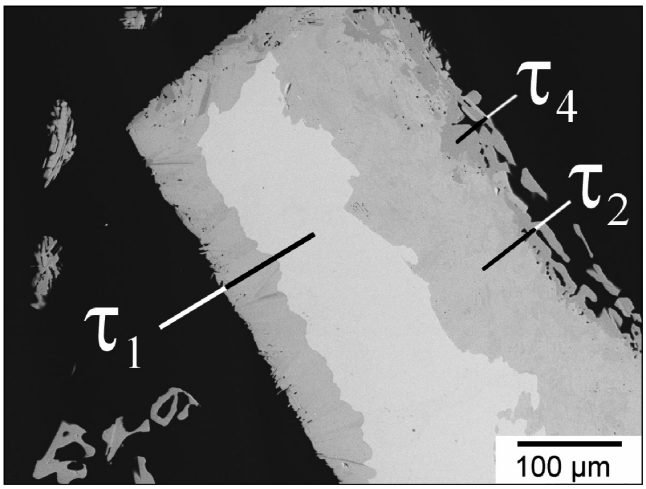

Fig. 7—Electron micrograph (BSE) of the sample $Al_{90}Ce_{2.6}Si_{7.4}$ (as-cast and subsequently 870 hours at 500 °C) showing the core of primary crystallized phase τ_1 (light gray) surrounded by the phase τ_2 (darker gray), formed in a peritectic (transition)-type reaction. The darker phase surrounding the phase τ_2 is considered to be the metastable phase τ_4.

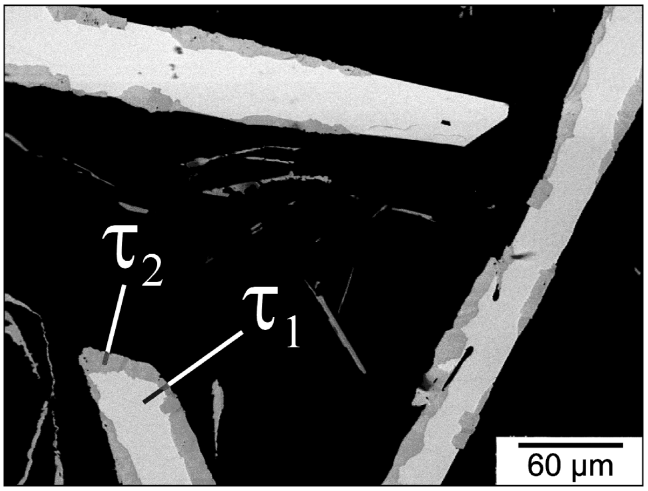

Fig. 8—Electron micrograph (BSE) of the same sample $Al_{90}Ce_{2.6}Si_{7.4}$ after being solidified at 5 K/min cooling rate during DSC measurement in Fig. 2. The core of primary crystallized phase τ_1 (light gray) is surrounded by the phase τ_2 (darker gray). This reflects the peritectic (transition)-type reaction, calculated at 621 °C in Table VI. That morphology is also observed in the as-cast microstructure in Fig. 7.

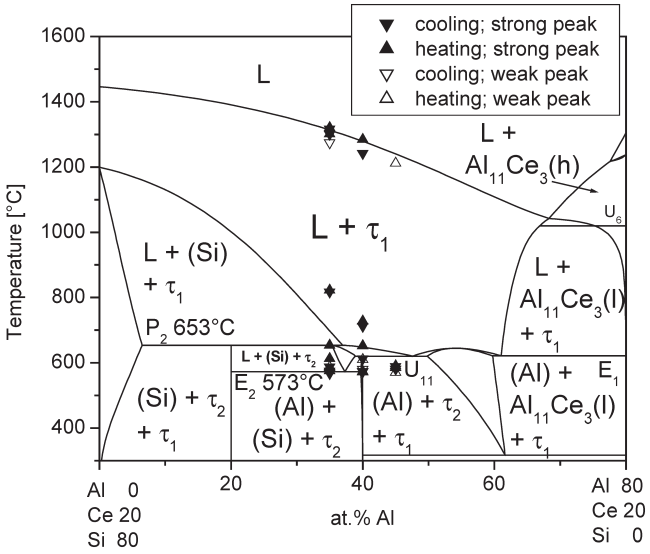

Fig. 9—Calculated vertical section $Ce_{20}Si_{80}$-$Al_{80}Ce_{20}$ at constant 20 at. pct Ce including the DTA signals measured in this work.

$Al_{90.0}Ce_{2.6}Si_{7.4}$ shows the primary crystallized phase τ_1 (light gray), which is surrounded by the later formed phase τ_2 (darker gray), which consumes the primary τ_1 in agreement with the calculated reaction L + τ_1 = τ_2 + (Al), U_{11}, at 621 °C (Figure 3). The small amount of the even darker phase adjoining the phase τ_2 is interpreted as the metastable phase τ_4. This phase was also found as fourth phase in small amounts in the samples $Al_{90.0}Ce_{3.2}Si_{6.8}$ and $Al_{90.0}Ce_{2.6}Si_{7.4}$ and is therefore interpreted as metastable.

In Figure 8 the microstructure of the $Al_{90.0}Ce_{2.6}Si_{7.4}$ sample solidified during DSC measurement at 5 K/min cooling rate is given. The phase sequence formed during solidification, primary τ_1 with some τ_2 formed at the periphery, is the same as in the as-cast sample in Figure 7; however, the amount of τ_2 formed is larger after the heat treatment. This reflects the calculated reaction L + τ_1 = τ_2 + (Al) at 621 °C, which remains incomplete during solidification. The corresponding DSC curve for this sample is given in Figure 2.

The thermal signals of the remaining three samples are displayed in Figure 9 along the section with constant 20 at. pct Ce. The sample $Al_{45}Ce_{25}Si_{30}$ is included here at 45 at. pct Al because it is close to that section. It exhibits a dendritic microstructure with large amounts of the primary crystallized phase τ_1, shown in Figure 10. At higher magnification, the additional phases τ_2 + (Al) are clearly detected, as expected from the calculated phase diagram.

The measured solidification enthalpies for the samples in the Al-rich corner are presented in the last row of Table V. These data are obtained by calibrated integration of the DSC heat flow *vs* time curves relative to a baseline of just the

solidification peak. This is shown for the example of alloy $Al_{90.0}Ce_{2.6}Si_{7.4}$ in Figure 2. In a separate measurement, the DSC signal from the empty crucible is determined and subsequently subtracted from the signal in Figure 2. This procedure results in a flat baseline with virtually zero differential heat flow before and after the reaction. After transforming the abscissa to the time scale, the integrated peak area thus corresponds to a latent heat of solidification (upper curve) or melting (lower curve). It is noted that these two values are very consistent. Even though the transition temperatures are substantially shifted and the signal shape is markedly different on cooling and heating, the integrated enthalpies in Figure 2 differ by only 0.12 kJ/mol.

For each composition listed in Table V, two samples are measured and a mean value is presented. Within the accuracy of measurement, no dependence of the solidification enthalpy on cooling rate (2 and 5 K/min) of the DSC analysis or the heating/cooling cycle sequence was observed. The DSC measurements show a high repeatability comparing different runs of the same sample (±0.10 kJ/mol, based on the maximum deviation), as well as good reproducibility comparing different samples of the same composition (±0.15 kJ/mol). The overall uncertainty of ±0.3 kJ/mol indicated in Table V includes both uncertainties mentioned previously and an estimated systematic error of measurement.

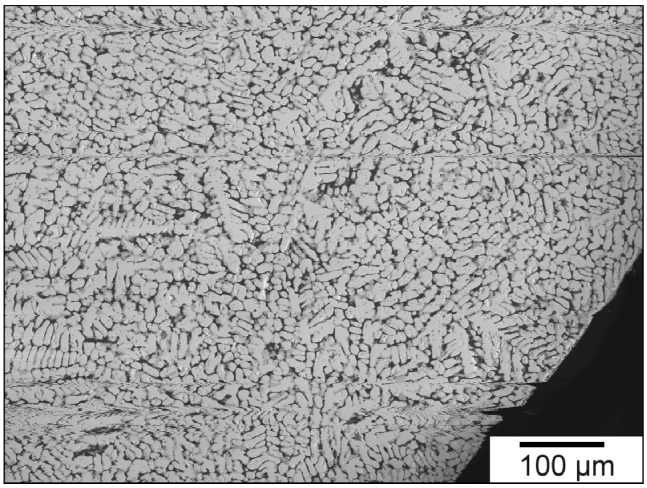

Fig. 10—Electron micrograph (BSE) of the sample $Al_{45}Ce_{25}Si_{30}$ (as-cast and subsequently 870 h at 500 °C) showing a dendritic microstructure of the primary crystallized phase τ_1.

D. *Thermodynamic Calculation*

The thermodynamic data sets for the binary subsystems Al-Ce[33] and Al-Si[34] were accepted as published. These data, together with the present Ce-Si, were used for the extrapolation and calculation of the ternary phase diagram and to select key samples for the investigation of the ternary system. The program Pandat,[22] used by Chen *et al.*,[35] was also used for all calculations in this work.

The liquid, fcc (Al, αCe), bcc (βCe), and diamond (Si) solution phases are described by the substitutional solution model. The ternary data are calculated using a Redlich–Kister/Muggianu type extrapolation from the binary sets,[36] with one ternary parameter for the excess term of the liquid phase:

$$^{E}G^{\text{tern,Liquid}} = L^{\text{Liquid}}_{\text{Al,Ce,Si}}\, x_{\text{Al}} x_{\text{Ce}} x_{\text{Si}} \qquad [4]$$

The Muggianu extrapolation for the ternary system is not unique. For strong asymmetric interactions, such as the weak Al-Si *vs* the strong Al-Ce and Ce-Si interaction, other extrapolation schemes might be more appropriate. The Redlich–Kister/Muggianu extrapolation was used for practical reasons.

The ternary phase τ_1 was modeled as a two-sublattice line compound $Ce_1(Al,Si)_2$ to reflect the experimentally observed ternary solubilities starting from the binary phase $CeSi_2$. The Gibbs energy (per mol of atoms) is expressed by

$$G^{\tau 1} = y_{\text{Al}} G^{0,\tau 1}_{\text{Ce:Al}} + y_{\text{Si}}\, G^{0,\tau 1}_{\text{Ce:Si}} + \frac{2}{3} RT(y_{\text{Al}} \cdot \mathbf{ln}\, y_{\text{Al}} + y_{\text{Si}} \cdot \mathbf{ln}\, y_{\text{Si}}) + y_{\text{Al}} \cdot y_{\text{Si}} \cdot L^{0,\tau l}_{\text{Ce:Al,Si}} + \ldots \qquad [5]$$

in which R is the gas constant, and y_{Al} and y_{Si} are the site fractions of Al and Si on the second sublattice. The parameter $G^{0,\tau 1}_{\text{Ce:Al}}$ (also called compound energy) expresses the Gibbs energy of the fictive binary stoichiometric compound $CeAl_2$ in $\alpha ThSi_2$ structure relative to the pure elements (Al-fcc, Ce-fcc, Si-diamond) at the same temperature. The parameter $G^{0,\tau 1}_{\text{Ce:Si}}$ represents the Gibbs energy of the stable binary compound $CeSi_2$ and is fixed from the binary Ce-Si data set. The interactions within the second sublattice of the τ_1 structure are modeled by the parameters $L^{0,\tau 1}_{\text{Ce:Al,Si}}$ and. The phases τ_2 and τ_3 are modeled as stoichiometric compounds, by simply extending Eq. [2] to the component Al.

The ternary parameters were determined using essentially the measured liquidus temperatures in the Al-rich corner combined with the information about the primary crystallizing phases. The parameters of the ternary phase τ_1 are optimized according to the measured liquidus temperatures,

Table V. Calculated Equilibrium Enthalpy Data (Figure 13) and Experimental Latent Solidification Enthalpy Extracted from the DSC Curves (Figure 2) for the Al-Rich Samples

Sample Composition in At. Pct	$Al_{90.0}Ce_{8.0}Si_{2.0}$	$Al_{90.0}Ce_{7.0}Si_{3.0}$	$Al_{90.0}Ce_{5.7}Si_{4.3}$	$Al_{90.0}Ce_{3.2}Si_{6.8}$	$Al_{90.0}Ce_{2.6}Si_{7.4}$
Calculated freezing range T_l to T_s (°C)	892 to 621	853 to 621	848 to 621	770 to 621	733 to 573
H (liquid, T_l) (kJ/mol)	−3.6	−4.9	−7.0	−9.2	−8.7
H (solid, T_s) (kJ/mol)	−24.5	−24.4	−26.5	−26.3	−27.3
ΔH_2 at T_l (kJ/mol)	−12.3	−12.2	−12.4	−12.2	−13.7
ΔH_1 at T_s (kJ/mol)	−11.3	−11.3	−12.1	−12.3	−13.1
Calculated latent solidification enthalpy $(\Delta H_1 + \Delta H_2)/2$ (kJ/mol)	−11.8 ± 0.5	−11.8 ± 0.5	−12.2 ± 0.2	−12.3 ± 0.1	−13.4 ± 0.3
Experimental latent solidification enthalpy (kJ/mol)	−12.2 ± 0.3	−12.5 ± 0.3	−12.6 ± 0.3	−12.6 ± 0.3	−12.6 ± 0.3

the observed extent of the primary crystallization, and the solid-state equilibria at 500 °C, especially the well-established tie-line from τ_1 to (Al).

The immiscibility of the τ_1 phase around 5 to 30 at. pct Al at 500 °C reported in References 28 and 29 is not modeled, since it would cause a bend of the τ_1-liquidus surface in the Al-rich region to higher temperatures that contradicts the experimental observations. The incongruent formation of τ_2 is given by the rather low DTA signal at 653 °C and, most importantly, by the peritectic formation type observed in the micrographs (*e.g.*, Figures 7 and 8). The decomposition of τ_2 above 650 °C was also observed by Flandorfer *et al.*[31] The ternary phase τ_4 is regarded to be not stable, based on the data of Reference 31 and our own results; it is therefore not included in the modeling. One ternary parameter for the liquid phase was used.

The calculated isothermal section of the Al-Ce-Si system at 500 °C is given in Figure 11. The investigated sample compositions are shown in different symbols according to the phase analysis. The arrows point to the measured phase compositions. The five additional samples along the 90 at. pct Al section are not shown here to enhance readability; they all support the calculated equilibria given in Figures 11 and 3.

Figure 3 shows the calculation of the vertical phase diagram section at constant 90 at. pct Al, which is important for the behavior of Al-rich alloys. These equilibria are compared to the DSC/DTA signals measured in this work. The calculated vertical section at constant 20 at. pct Ce is given in Figure 9. The DTA signals from the samples $Al_{35}Ce_{20}Si_{45}$ and $Al_{40}Ce_{20}Si_{40}$ are given in this section. In addition, the results of sample $Al_{45}Ce_{25}Si_{30}$ are shown, although the composition of this sample is slightly more Ce rich.

The calculated liquidus surface is shown in Figure 12. It is dominated by the primary field of phase τ_1 in agreement with all investigated samples. The two other ternary phases, τ_2 and τ_3, are solidified as primary crystals only in small regions at the edge of the large τ_1 primary phase region. The calculated invariant reactions involving the liquid phase are compiled in Table VI. The four invariant reactions that are important in the Al-rich corner were also observed experimentally in good agreement with the calculations. The assessed parameters for the binary Ce-Si and ternary Al-Ce-Si system are given in Table VII.

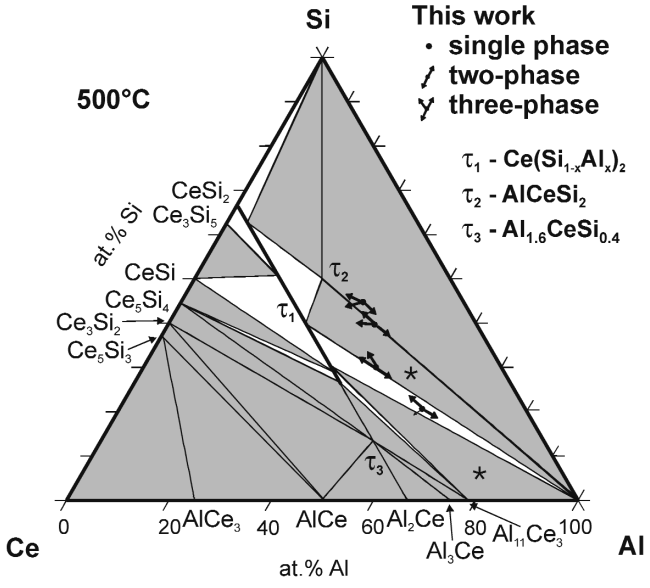

Fig. 11—The calculated isothermal section of the Al-Ce-Si system at 500 °C. Dots represent the investigated samples compositions; arrows point to the identified phases. Three-phase triangles are shaded. Those marked by an asterisk (*) are also firmly established by literature data and the present five additional samples along the 90 at. pct Al section.

For the Al-rich samples, the heat evolution during solidification is calculated using equilibrium conditions. It is not trivial to extract a "latent" heat of solidification, which may then be compared to the DSC measurement. Because of the extended temperature range of solidification, the calculated enthalpy differences have to be corrected by subtracting the contribution arising from the heat capacity. The scheme is exemplified in Figure 13 for the equilibrium solidification of alloy $Al_{90.0}Ce_{2.6}Si_{7.4}$, and the pertinent data are given in Table V for all alloys as detailed subsequently.

The complete equilibrium solidification involves the five successive phase fields denoted in Figure 13, and during that process, the alloy releases the total heat ΔH^{total} between liquidus (T_l) and solidus (T_s) temperature:

$$\Delta H^{\text{total}} = H\,(\text{solid}, T_s) - H\,(\text{liquid}, T_l) \qquad [6]$$

One possibility to calculate a latent heat is to supercool the liquid down to T_s, using the known heat capacity of the liquid, and then to solidify isothermally at T_s to the equilibrium phases, resulting in a latent heat:

$$\Delta H_1 = H\,(\text{solid}, T_s) - H\,(\text{liquid}, T_s) \qquad [7]$$

Another possibility is to solidify the liquid at T_l to the superheated solid phases, which are subsequently cooled to T_s, resulting in a different latent heat:

$$\Delta H_2 = H\,(\text{solid}, T_l) - H\,(\text{liquid}, T_l) \qquad [8]$$

Even though the first path suggested in Eq. [6] may appear more natural, it is in no way unique. The second path or even an isothermal solidification step at any intermediate temperature between T_l and T_s may be justified as well. The average of both paths may be taken to be the latent heat of

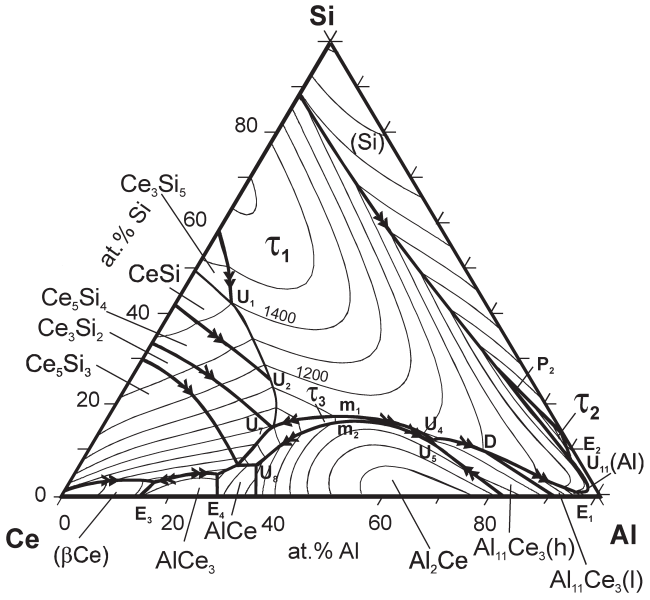

Fig. 12—Calculated Al-Ce-Si liquidus surface.

Table VI. The Calculated Ternary Invariant Reactions Involving Liquid Phase Compared to the Experiment Data

Invariant Reaction		Experimental (This Work)	Calculated (This Work)		
	Type	T (°C)	T (°C)	x^L (Al)	x^L (Si)
$L + Ce_5Si_3 = \tau_1 + CeSi$	U_1	—	1398	0.1075	0.4193
$L = \tau_1 + \tau_3$	m_1	—	1136	0.5082	0.1616
$L + Al_2Ce + Al_{11}Ce_3$ (h) $= Al_3Ce$	P_1	—	1135	0.6556	0.0992
$L = Al_2Ce + \tau_3$	m_2	—	1134	0.5169	0.1575
$L + CeSi = Ce_5Si_4 + \tau_1$	U_2	—	1132	0.2611	0.2516
$L + Al_2Ce = Al_3Ce + \tau_3$	U_3	—	1100	0.6282	0.1188
$L + Al_3Ce = \tau_3 + Al_{11}Ce_3$ (h)	U_4	—	1099	0.6293	0.1188
$L + \tau_3 = \tau_1 + Al_{11}Ce_3$ (h)	U_5	—	1079	0.6379	0.1244
$L + \tau_1 + Al_{11}Ce_3$ (h) $= Al_{11}Ce_3$ (l)	D	—	1020	0.7097	0.1086
$L + \tau_1 = \tau_3 + Ce_5Si_4$	U_6	—	895	0.3181	0.1503
$L + Ce_5Si_4 = \tau_3 + Ce_3Si_2$	U_7	—	889	0.3172	0.1477
$L + Al_2Ce = \tau_3 + AlCe$	U_8	—	730	0.3268	0.0667
$L + \tau_1 + (Si) = \tau_2$	P_2	653	653	0.6571	0.2895
$L + Ce_3Si_2 = \tau_3 + Ce_5Si_3$	U_9	—	645	0.2922	0.0680
$L + \tau_3 = AlCe + Ce_5Si_3$	U_{10}	—	628	0.2908	0.0640
$L = \tau_1 + (Al)$	m_3	—	644	0.9702	0.0174
$L + \tau_1 = \tau_2 + (Al)$	U_{11}	621	621	0.9083	0.0788
$L = (Al) + \tau_1 + Al_{11}Ce_3$ (l)	E_1	633	621	0.9631	0.0042
$L = \tau_2 + (Al) + (Si)$	E_2	572	573	0.8371	0.1515
$L = Ce_5Si_3 + AlCe_3$	m_4	—	572	0.2280	0.0433
$L = Ce_5Si_3 + AlCe_3 + (\alpha Ce)$	E_3	—	553	0.2655	0.0452
$L = AlCe + Ce_5Si_3 + AlCe_3$	E_4	—	537	0.1615	0.0273

Table VII. Parameters Assessed in This Work for the Binary Ce-Si and the Ternary Al-Ce-Si System in J/mol of Atoms

Liquid phase:

$$L^{0,\text{Liquid}}_{\text{Ce,Si}} = -99{,}974.63 - 61.61*T$$
$$L^{1,\text{Liquid}}_{\text{Ce,Si}} = -63{,}423 + 90.35*T$$
$$L^{\text{Liquid}}_{\text{Al,Ce,Si}} = -400{,}000$$

Ce-Si binary compounds:

$$G^{\text{Ce5Si3}}_{\text{Ce:Si}} = -61{,}000 + 4*T + 0.625\,G^{0,\text{fcc}}_{\text{Ce}} + 0.375\,G^{0,\text{diamond}}_{\text{Si}}$$
$$G^{\text{Ce3Si2}}_{\text{Ce:Si}} = -65{,}000 + 4.785*T + 0.6\,G^{0,\text{fcc}}_{\text{Ce}} + 0.4\,G^{0,\text{diamond}}_{\text{Si}}$$
$$G^{\text{Ce5Si4}}_{\text{Ce:Si}} = -69{,}000 + 4.515*T + 0.555556\,G^{0,\text{fcc}}_{\text{Ce}} + 0.444444\,G^{0,\text{diamond}}_{\text{Si}}$$
$$G^{\text{CeSi}}_{\text{Ce:Si}} = -71{,}100 + 3.305*T + 0.5\,G^{0,\text{fcc}}_{\text{Ce}} + 0.5\,G^{0,\text{diamond}}_{\text{Si}}$$
$$G^{\text{Ce3Si5}}_{\text{Ce:Si}} = -65{,}000 - 3.53*T + 0.375\,G^{0,\text{fcc}}_{\text{Ce}} + 0.625\,G^{0,\text{diamond}}_{\text{Si}}$$

$Ce(Si_{1-x}Al_x)_2$ (τ_1):

$$G^{\text{CeSi2}}_{\text{Ce:Si}} = -60{,}500 - 6.047*T + 0.333333\,G^{0,\text{fcc}}_{\text{Ce}} + 0.666667\,G^{0,\text{diamond}}_{\text{Si}}$$
$$G^{\text{CeSi2}}_{\text{Ce:Al}} = -50{,}000 + 12*T + 0.333333\,G^{0,\text{fcc}}_{\text{Ce}} + 0.666667\,G^{0,\text{fcc}}_{\text{Al}}$$
$$L^{0,\text{CeSi2}}_{\text{Ce:Al,Si}} = -48{,}000 + 20*T$$
$$L^{1,\text{CeSi2}}_{\text{Ce:Al,Si}} = -24{,}000 + 30*T$$

$AlCeSi_2$ (τ_2):

$$G^{\text{AlCeSi2}}_{\text{Al:Ce:Si}} = -65{,}600 + 15*T + 0.25\,G^{0,\text{fcc}}_{\text{Al}} + 0.25\,G^{0,\text{fcc}}_{\text{Ce}} + 0.5\,G^{0,\text{diamond}}_{\text{Si}}$$

$Al_{1.6}CeSi_{0.4}$ (τ_3):

$$G^{\text{Al1.6CeSi0.4}}_{\text{Al:Ce:Si}} = -67{,}000 + 15*T + 0.533333\,G^{0,\text{fcc}}_{\text{Al}} + 0.333333\,G^{0,\text{fcc}}_{\text{Ce}} + 0.133333\,G^{0,\text{diamond}}_{\text{Si}}$$

solidification of this alloy, as justified as follows in comparison to the experimental data:

$$\Delta H^{\text{latent}} = (\Delta H_1 + \Delta H_2)/2 \quad [9]$$

The experimental latent heat of solidification, compiled in the last row of Table V, is obtained by integration of the differential heat flow, as detailed in Section III–C and Figure 2. The fact that the slightly varying heat capacity differences before and after the reaction are averaged during integration of the DSC signal is therefore properly accounted for by using Eq. [9].

In order to calculate $\Delta H_3 = H$ (solid, T_s) $- H$ (solid, T_l), the heat capacity of the mixture of the solidified phases was simply taken to be the same as that of pure (Al). This is justified since these alloys consist of 90 pct (Al) phase, and the superheated phases may not have a well-defined heat capacity. Table V shows all the relevant enthalpy data for the five alloys on the 90 at. pct Al section.

IV. DISCUSSION

A. *The Binary Ce-Si System*

The present modeling of the binary system Ce-Si is mainly based on the melting temperatures measured by

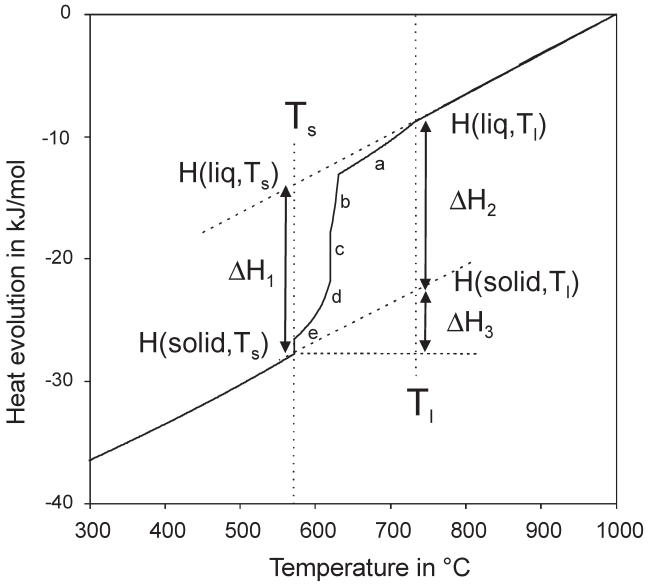

Fig. 13—Calculated total equilibrium enthalpy of the alloy $Al_{90.0}Ce_{2.6}Si_{7.4}$ (solid curve). Starting value zero at 1000 °C is set arbitrarily for this figure. Dashed lines are metastable extrapolations of liquid, supercooled below T_l, and the solid, superheated above T_s. (a) through (e) correspond to the five different phase fields seen during solidification of this alloy, as in Fig. 3: (*a*) L + τ_1, (*b*) L + τ_1 + (Al), (*c*, U_{11}) L + τ_1 = τ_2 + (Al), (*d*) L + τ_2 + (Al), and (*e*, E_2) L = τ_2 + (Al) + (Si) (also Fig. 2).

Table VIII. Integral Enthalpy of Mixing in the Liquid Ce-Si Phase at 1650 °C[18,19] and 1617 °C[20] Compared to Calculated Data at 1650 °C, in kJ/Mol Atoms

x (Si)	Δ*H* Ryss *et al.*[18]	Δ*H* Sudavtsova *et al.*[20]	Δ*H* Calculated (This Work)
0	0	—	0
0.05	−10.3	—	−7.5
0.1	−20.5	—	−13.6
0.15	−30.4	—	−18.4
0.2	−39.8	—	−22.1
0.25	−48.6	—	−24.7
0.3	−56.6	—	−26.3
0.35	−63.3	—	−27.1
0.4	−68.4	—	−27.04
0.45	−72.0	—	−26.3
0.5	−73.9	—	−24.9
0.52	−74.0	—	−24.3
0.55	−73.75	—	−23.2
0.6	−71.3	—	−20.9
0.65	−66.7	—	−18.4
0.7	−60.2	—	−15.7
0.75	−52.3	—	−12.8
0.8	−43.3	−45	−9.9
0.85	−33.4	−35	−7.1
0.9	−22.8	−23	−4.4
0.95	−11.65	−11	−2.0
1	0	0	0

Benesovsky *et al.*[10] and the enthalpies of formation by Meschel and Kleppa.[16,17] Benesovsky *et al.*[10] acknowledged systematic displacement of the concentration of their samples due to formation of cerium oxide. This oxide was shown in a micrograph forming small gray plates.[10] Since the determination of the melting temperatures was performed by observing the melting of Seger-cone formed samples, the existence of visible oxide grains might have significantly influenced the accuracy of the measurement. The absence of information about the number of samples and their composition renders the interpretation of the experimental data as done in Reference 10 questionable. Therefore, only the measured melting temperatures have been adopted in the present study, as shown in Figure 1. The originally plotted phase diagram[10] with deeply notched eutectics between high congruent melting points of the intermetallic phases is thermodynamically very unlikely. The present interpretation of the observed melting temperatures as peritectic formation of the intermediate phases melting below $CeSi_2$ is more realistic because of the calculation from a consistent set of smooth thermodynamic functions.

The absolute values of the standard entropies, S^0_{298}, of the six compounds obtained in the present assessment are given in Table I. These S^0_{298} values show very reasonable values ranging between the pure components from $S^0_{298}(\alpha Ce)$ = 69.2 to $S^0_{298}(Si)$ = 18.7 J/mol K, thus supporting the present assessment. The fact that enthalpies of formation[16] of two important compounds, $CeSi_2$ and CeSi, could be used for the thermodynamic modeling is another strong point. The experimental value for Ce_5Si_3 is less negative than the calculated value; however, accepting the experimental enthalpy value[17] exactly would result in a drastically lower melting temperature of Ce_5Si_3, well below the experimental data given in Reference 10. Because of the smooth composition dependence of all the assessed enthalpies of formation in Table I, this would also impose deviations in the other melting temperatures. In the frame of the subregular solution model, considered reasonable for the current limited knowledge of this liquid phase, this discrepancy between enthalpy and melting temperature cannot be reconciled for the Ce-richest compound Ce_5Si_3.

The measured enthalpies of mixing of the liquid phase by Ryss *et al.*[18,19] and Sudavtsova *et al.*[20] were not used for the optimization. These values are incompatible with the measured enthalpies of formation of the solid phases and their melting points. They are also much more negative compared to related binary Ce-Ni and Ce-Cu systems.[20] If one accepts this large negative mixing enthalpy for liquid[18,19,20] together with the liquidus temperatures and reasonable entropies, then the calculated enthalpies of formation of the solid phases are entirely off the experimental data. We prefer to use the experimental solid phase data of Meschel and Kleppa[16] in our assessment. This marked inconsistency in the experimental data of the Ce-Si system could only be revealed by such a Calphad-type analysis, and it is detailed in Table VIII, comparing the experimental data reported[18,19,20] to the present assessment. Additional experimental work is needed to resolve this inconsistency.

B. *Ternary Al-Ce-Si Phase Equilibria*

All available experimental data are well described by the calculated ternary phase diagram Al-Ce-Si. The main attention in this work is drawn to the Al-rich corner and the phases in equilibrium with the (Al) phase. In this area, the calculation produces a satisfying agreement with experimental data, indicating well-defined Gibbs energy data sets of all pertinent phases. The experimentally found liquidus

in the center of the phase diagram is reproduced properly, even though the single ternary liquid interaction parameter was fitted only to the experimental data at 90 at. pct Al. The calculated liquidus surface is also in perfect agreement with the observed primary crystallizing phases of all samples (Table III) and the solidification sequence found in the micrographs.

This agreement between the sequence of phase formation and corresponding microstructures and the calculated phase diagram is considered to be very important. Comparison of Figures 3 and 9 with the corresponding microstructures shows that the range of primary solidification provides a strong constraint and check for the thermodynamic modeling. This is at least as important as the immediately visible comparison to the DSC/DTA signals in Figures 3 and 9. Similarly important are the secondary and subsequent reactions during cooling, as detailed for the example of sample $Al_{90.0}Ce_{2.6}Si_{7.4}$ in Section III–C and Figures 7 and 8 in comparison to Figure 3. This confirms the calculated reaction L + τ_1 = τ_2 + (Al) at 621 °C, which remains incomplete during solidification.

The miscibility gap in the τ_1 phase, reported in References 28 and 29 at 500 °C, is not modeled in this work. For that region, remote from the equilibrium with (Al), improvement of the thermodynamic data set may be possible. More experimental data, however, are needed in that region before a refinement of modeling will make sense.

Phase τ_4, reported by References 28 and 29, could not be observed in this work and is assumed to be not stable, confirming the conclusion of Reference 31. Phase τ_5 reported by Reference 30 after long annealing (336 hours) at 500 °C is not observed in this work. A phase of this composition and crystal structure could not be detected in the investigated sample compositions, neither using EDX nor XRD, although our samples were heat treated for an even longer time (870 hours) at 500 °C.

C. *Heat of Solidification of Ternary Alloys*

As shown in Section III–D, it is not trivial to separate the heat of solidification of alloys with a wide freezing range into a latent part and a heat capacity contribution. However, only the former may be compared to the experimental DSC data, obtained from an integrated DSC-peak area. The agreement between the calculated and experimental data shown in Table V is acceptable. This independent measurement is an additional support of the present thermodynamic description of the Al-Ce-Si system, despite the difficulties in calculating the latent heat values. Even the slight increase of the absolute value with Si content is reflected in both the calculated and experimental enthalpy data. This agreement is not hampered by the fact that some transition reactions did not go to completion, *e.g.*, in Figure 8, because the corresponding solid-state reactions involve only small enthalpies of transition.

It is emphasized that for each sample, the latent heats of solidification and melting are very consistent. That is, in properly conducted experiments, the total heat effects are the same and not dependent on heating/cooling rates or the observed supercooling of some transition temperatures.

It is noted that the uncertainty of the *calculated* values, given as half of the difference between ΔH_1 and ΔH_2 in Table V, may be even larger than the overall experimental uncertainty. This difference stems from the fact that the average heat capacity of liquid is generally different from that of the solid phases in that temperature range. Therefore, the separated latent part must be different for the two hypothetical solidification paths of ΔH_2 at T_l compared to that of ΔH_1 at T_s. A unique value of ΔH^{latent} could therefore not be calculated, and the mean value given in Table V is only a simplification.

An additional uncertainty in the calculation is due to the not well-known heat capacities of both the supercooled liquid and the superheated solid phases. Supercooled liquid phases may exhibit an intricate C_p function, as is well known for the example of glass forming alloys. Since there is no such detailed C_p data available for Al-Ce-Si alloys, a simple extrapolation, based on the Gibbs energy equation of the stable ternary liquid, was used. For superheated solid phases, that type of uncertainty might be even larger. Since the solidified phase assembly consists mostly of (Al), the hypothetical solidification path of ΔH_2 requires the formation of this substantially above the stability limit of 660 °C for the (Al) phase. Even so, the experimental data are in better agreement with this ΔH_2 step for all but the two Si-richest alloys as compared to the ΔH_1 step. It appears that the heat capacity contribution depicted as ΔH_3 in Figure 11 is reasonably estimated in the present approach.

Finally, it should be noted that the molar fraction of the liquid phase amount at a given temperature within the freezing range cannot be read from Figure 13 by taking the fraction $\{H(T) - H(\text{solid}, T)\}/\{H(\text{liquid}, T) - H(\text{solid}, T)\}$. This would require use of the molar enthalpy of the residual equilibrium liquid instead of H (liquid, T), the molar enthalpy of the supercooled liquid at initial composition. These two values may be substantially different, as clearly shown by Dong *et al.*[37] This is because the liquid composition during the actual equilibrium solidification will move and its path may be mapped onto the liquidus surface in Figure 14, for example, from $Al_{90.0}Ce_{2.6}Si_{7.4}$ all the way down to E_2. However, for the calculation of, at least, an average value of latent heat, the quantities shown dashed in Figure 13 have

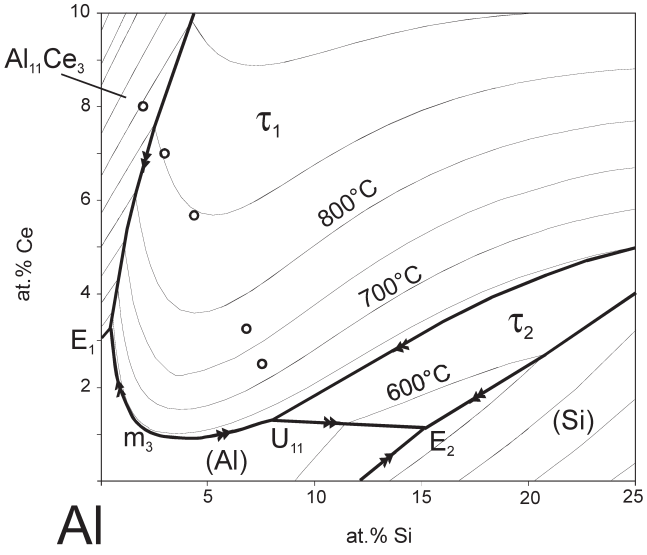

Fig. 14—Calculated Al corner of Al-Ce-Si liquidus surface. Open circles represent investigated sample compositions (Fig. 3).

to be used because only they allow the isothermal transformation of the entire liquid phase to a complete solid state. We agree with Dong *et al*.[37] that the only way to accurately obtain the fraction of liquid from the measured enthalpy is *via* a model of microsegregation.

In summary, even though the equilibrium enthalpy function of Al-rich ternary Al-Ce-Si alloys is well established from the consistent thermodynamic description, the splitting of the overall enthalpy of solidification in a latent part and a heat capacity contribution over the freezing range poses a fundamental problem. This splitting cannot be done in a unique way. The uncertainty in alternative calculated values may be even larger than the experimental uncertainty, as determined in the present calorimetric measurements.

D. *Thermodynamic Aspects of Grain Refining Effects of Ce in Al-Si Alloys*

The ternary phase diagrams calculated from the thermodynamic description are, at least in the Al-rich region of the ternary system, consistent and well supported by experimental data. It is thus considered safe to use these diagrams, especially the liquidus surface pertinent to Al-Si casting alloys with small additions of Ce shown in Figure 14, for a discussion of the grain refining potential of cerium. The aim of this discussion is to quantitatively identify the possible contributions due to the phase equilibria. Other important, though still controversial, aspects of grain refining[2] will not be discussed here.

Figure 14 shows that small Ce addition could provide ternary high-temperature stable τ_1 and τ_2 phases in equilibrium with Al-Si–rich melt. These phases might act as nucleation sites for (Al) or (Si) crystals in both hypo- and hypereutectic Al-Si alloys. In addition, the liquidus temperature of primary (Al) is slightly, and that of primary (Si) is drastically, reduced by the addition of Ce, thus reducing the growth temperature of (Si) crystals. It should be noted that the ternary eutectic, E_2, is shifted to substantially higher Si content compared to the binary Al-Si eutectic.

The practical grain refining effect of RE in Al-Si alloys was not studied by addition of pure Ce but of mischmetal, consisting mainly of Ce. In the studies of Chang *et al*.,[7,8] the three main components were 51Ce-25La-14Nd (mass pct). For comparison with our Al-Ce-Si phase diagrams, we will count the total RE addition as pure "Ce," which is clearly an approximation, though reasonable in view of the chemical similarity of Ce and La.

The hypereutectic Al-21Si alloy was studied with nominal additions of 0, 1, 2, and 3 mass pct RE (0, 0.19, 0.37, and 0.58 at. pct "Ce").[7] A substantial grain refining effect on primary (Si), especially at the lowest cooling rate of 33 K/s, was observed, as was a modification of eutectic silicon. In addition, a depression of the primary (liquidus) temperature of 12 to 17 K for 1 to 3 pct RE addition was measured by DTA with 2 K/min cooling rate.[7] This trend is in good agreement with our calculated slope of the liquidus line along that section, −6 K/mass pct Ce. Similarly, a depression of the eutectic temperature was measured, but the reported value is unclear; 2 to 7 K are given in the text and 7 to 8 K are read from the diagram.[7] The former value agrees well with our calculated temperature difference of 4 K between the binary Al-Si eutectic and the ternary eutectic E_2.

The RE–rich particles containing mainly Al, Si, and Ce with trace amounts of La, Nd were also detected by SEM/EDS analysis. Selected area diffraction patterns of one particle taken in a TEM could be indexed as the orthorhombic AlCe structure.[7] This, however, is inconsistent with the present Al-Ce-Si phase diagram, where ternary phases containing all three elements in an orthorhombic structure are unknown. Only tetragonal or hexagonal structures are known, as given in Table II, even if the metastable phases τ_4 and τ_5 are included. This is also inconsistent with data from the same alloy (Al-21Si-2RE) in another article from the same group,[8] where the particles were interpreted by wavelength dispersive spectrometry (WDS) data as Al_2Si_2RE, which would correspond to the present metastable hexagonal phase τ_4. In addition to these particles, RE-enriched zones of 2- to 4-μm width in the matrix between (Si) crystals were found, containing 5 mass pct Ce and 2 mass pct La.[8] These zones could correspond to finely dispersed ternary phases τ_2 or τ_1, if the Ce + La contents were lumped together. The maximum solubility of RE measured in the (Si) crystal corresponds to 0.05 at. pct "Ce,"[8] which supports the negligible solubility range in (Si) of the present thermodynamic model.

In an attempt to explain the grain refining effect, Chang *et al*.[7] assume that the compound AlCe solidifies in the melt prior to the solidification of primary (Si) because of its higher melting point. By contrast, the liquidus surface in Figure 12 shows that primary solidification of AlCe should only occur in a small region at extremely high Ce content above 60 at. pct Ce and certainly not in the investigated alloys with only up to 0.58 at. pct "Ce." The explanation put forward by Chang *et al*.[7] follows the critical growth temperature hypothesis, suggesting that the nucleation of silicon is suppressed to the temperature of globular growth by the addition of RE. This would be in agreement with the present ternary phase diagram and the slope of the liquidus surface of (Si) as detailed previously.

For the hypoeutectic Al-7Si-0.3Mg (mass pct) alloy, the effect of 0.25 to 1.5 mass pct RE mischmetal additions on modification of eutectic (Si) and its correlation with properties was studied by Ravi *et al*.[9] They also report an evident reduction of the secondary dendrite arm spacing, *i.e*., grain refining of the primary (Al). The effects were most beneficial for an addition of 1 mass pct RE. The RE-bearing particles detected in their study are of complex composition, partly also containing Mg and Fe but only little RE, below 4 at. pct Ce and 1.6 at. pct La.[9] This finding is not reflected by any of the ternary Al-Ce-Si compounds of the present study.

An important conclusion from the phase diagram is that only the two ternary phases τ_1 and τ_2 are formed in equilibrium with typical Al-Si cast alloys as shown clearly in the liquidus surface in Figure 14 and also in the overview of Figure 12. Truly binary phases, especially the Ce-silicides, do not play a role. The binary $Al_{11}Ce_3$ is only formed upon Ce addition to almost pure aluminum with less than 0.5 at. pct Si. Beyond this limit τ_1 and τ_2 (beyond 8 at. pct Si) are formed, as shown in Figure 14. This domination of τ_1 and τ_2 is also seen in the solid state equilibria, Figure 11. This figure also shows that even though τ_1 originates as a solid solution from binary $CeSi_2$, it contains more than 27 at. pct Al in equilibrium with (Al). The binary AlCe phase is far from being in equilibrium with (Al) or (Si). At high temperatures, the phase τ_1 becomes most important and even replaces τ_2 in equilibrium

with Si-rich melts. Cerium could thus in principle be used for a primary solidification of τ_1 or τ_2 and its subsequent effect as a nucleation site. The additions necessary, however, are too high (>1 at. pct Ce or >5 mass pct Ce) and costly for a practical application following this nucleant grain refining route. By contrast, the substantial lowering of the liquidus temperature, and, thus, the growth temperature, of (Si) by Ce addition appears promising.

ACKNOWLEDGMENT

This study is supported by the German Research Foundation (DFG) in the priority programme "DFG-SPP 1120: Phase transformations in multi-component melts" under Grant No. Schm 588/24.

REFERENCES

1. S.A. Kori, B.S. Murty, and M. Chakraborty: *Mater. Sci. Eng. A*, 2000, vol. 283, pp. 94-104.
2. M. Easton and D. St. John: *Metall. Mater. Trans. A*, 1999, vol. 30A, pp. 1613-23.
3. M. Easton and D. St. John: *Metall. Mater. Trans. A*, 1999, vol. 30A, pp. 1625-33.
4. S.A. Kori, B.S. Murty, and M. Chakraborty: *Mater. Sci. Technol*., 1999, vol. 15, pp. 986-92.
5. W. Vogel and W. Schneider: *Giesserei*, 1991, vol. 78, pp. 848-53.
6. C.R. Ho and B. Cantor: *Acta Metall. Mater*., 1995, vol. 43 (8), pp. 3231-39.
7. J. Chang, I. Moon, and C. Choi: *J. Mater. Sci*., 1998, vol. 33, pp. 5015-23.
8. J. Chang, G.H. Kim, I.G. Moon, and C. Choi: *Scripta Mater*., 1998, vol. 39. pp. 307-14.
9. M. Ravi, U.T.S. Pillai, B.C. Pasi, A.D. Damodaran, and E.S. Dwarakadasa: *Metall. Mater. Trans. A*, 1996, vol. 27A, pp. 1283-92.
10. F. Benesovsky, H. Nowotny, W. Pifger, and H. Rassaerts: *Monatsh. Chem*., 1966, vol. 97, pp. 221-29.
11. K.A. Gschneidner, Jr. and M.E. Verkade: *Selected Cerium Phase Diagrams*, Doc. IS-RIC-7, Iowa State University, Ames, IA, 1974, pp. 36-37.
12. T.B. Massalski, P.R. Subramanian, H. Okamoto, and L. Kacprzak: *Binary Alloy Phase Diagrams*, 2nd ed., ASM INTERNATIONAL, Materials Park, OH, 1990, vol. 2, pp. 1110-12.
13. L.A. Dvorina: *Izv. Akad. Nauk SSSR, Neorg. Mater*., 1965, vol. 1 (10), pp. 1772-17 (translation: *Inorg. Mater*., 1965, vol. 1, pp. 1604-08).
14. L. Brewer and D. Krikorian: *J. Electrochem. Soc*., 1956, vol. 103 (38–51), pp. 701-03.
15. H. Yashima, T. Satoh, H. Mori, D. Watanage, and T. Ohtsuka, *Solid State Commun*., 1982, vol. 41 (1), pp. 1-4.
16. S.V. Meschel and O.J. Kleppa: *J. Alloys Compounds*, 1995, vol. 220, pp. 88-93.
17. S.V. Meschel and O.J. Kleppa: *J. Alloys Compounds*, 1996, vol. 243, pp. 186-93.
18. G.M. Ryss, Y.O. Esin, A.I. Stroganov, and P.V. Gel'd: *Z. Phys. Khim*., 1977, vol. 51 pp. 232-33 (translation: *Russ. J. Phys. Chem*. 1977, vol. 51, pp. 134-35).
19. G.M. Ryss, Y.O. Esin, M.S. Petrushevskii, A.I. Stroganov, and P.V. Gel'd: *Z. Phys. Khim*., 1979, vol. 53, pp. 1352-53 (translation: Russ. *J. Phys. Chem*., 1979, vol. 53, p. 767).
20. V.S. Sudavtsova, Y.G. Gorobec, and G.I. Batalin: *Rasplavy*, 1988, vol. 2 (6), pp. 79-81.
21. A.T. Dinsdale: *Calphad*, 1991, vol. 15, pp. 317-425.
22. *Pandat—Phase Diagram Calculation Engine for Multicomponent Systems*, CompuTherm LLC, Madison, WI, 2000.
23. G. Brauer and H. Haag: *Z. Anorg. Chem*., 1952, vol. 267, pp. 198-212.
24. O.S. Zarechnyuk: *Zb. Rob. Asp. L'vov Univ. Pri., Nauk L'vov*, 1963, pp. 15-20.
25. L.N. Altunina, E.I. Gladyshevsky, O.S. Zarechnyuk, and I.F. Kolobnev: *Z. Neorg. Khim*., 1963, vol. 8, pp. 870-73.
26. A. Raman: *Z. Metallkd*., 1967, vol. 58 (3), pp. 179-84.
27. A. Raman and H. Steinfink: *Inorg. Chem*., 1967, vol. 6, pp. 1789-95.
28. A.A. Murav'eva: *Autoreferat Dis. Kand. Khim., Nauk L'vov*, 1972, pp. 1-18 (abstract of thesis).
29. A.A. Murav'eva, O.S. Zarechnyuk, and E.I. Gladishevskii: *Visn. L'viv. Univ., Ser. Khim*., 1972, vol. 13, pp. 14-17.
30. H. Flandorfer and P. Rogl: *J. Solid State Chem*., 1996, vol. 127, pp. 308-14.
31. H. Flandorfer, D. Kaczorowski, J. Gröbner, P. Rogl, R. Wouters, C. Godart, and A. Kostikas: *J. Solid State Chem*., 1998, vol. 137, pp. 191-205.
32. G.W.H. Höhne, W. Hemminger, and H.-J. Flammersheim: *Differential Scanning Calorimetry: an Introduction for Practitioners*, Springer-Verlag, Berlin, 1996, pp. 103-04.
33. G. Cacciamani and R. Ferro: *Calphad*, 2001, vol. 25, pp. 583-97.
34. J. Gröbner, H.-L. Lukas, and F. Aldinger: *Calphad*, 1996, vol. 20 (2), pp. 247-54.
35. S.-L. Chen, S. Daniel, F. Zhang, Y.A. Chang, W.A. Oates, and R. Schmid-Fetzer: *J. Phase Equilibria*, 2001, vol. 22 (4), pp. 373-78.
36. R. Schmid-Fetzer and J. Gröbner: *Adv. Eng. Mater*., 2001, vol. 3 (12), pp. 947-61.
37. H.B. Dong, M.R.M. Shin, E.C. Kurum, H. Cama, and J.D. Hunt: *Metall. Mater. Trans. A*, 2003, vol. 34A, pp. 441-47.
38. A. Munitz, A.B. Gokhale, and G.I. Abbaschian: *Bull. Alloy Phase Diagrams*, 1989, vol. 10 (1), pp. 73-78.